TERRAFM: A SCALABLE FOUNDATION MODEL FOR UNIFIED MULTISENSOR EARTH OBSERVATION

Anonymous authors
Paper under double-blind review

ABSTRACT

Modern earth observation (EO) increasingly leverages deep learning to harness the scale and diversity of satellite imagery across sensors and regions. While recent foundation models have demonstrated promising generalization across EO tasks, many remain limited by the scale, geographical coverage, and spectral diversity of their training data, factors critical for learning globally transferable representations. In this work, we introduce **TerraFM**, a scalable self-supervised learning model that leverages globally distributed Sentinel-1 and Sentinel-2 imagery, combined with large spatial tiles and land-cover aware sampling to enrich spatial and semantic coverage. By treating sensing modalities as natural augmentations in our self-supervised approach, we unify radar and optical inputs via modality-specific patch embeddings and adaptive cross-attention fusion. Our training strategy integrates local-global contrastive learning and introduces a dual-centering mechanism that incorporates class-frequency-aware regularization to address long-tailed distributions in land cover. TerraFM achieves strong generalization on both classification and segmentation tasks, outperforming prior models on GEO-Bench and Copernicus-Bench. Our code and pretrained models will be publicly released.

1 INTRODUCTION

EO provides systematic measurements of the surface of earth, supporting a wide spectrum of critical applications such as land use monitoring Wang et al. (2023), crop evaluation Prodhan et al. (2021); Kussul et al. (2017), urban development Yu & Fang (2023), and disaster response Huot et al. (2022); Sarkar et al. (2023); Rahnemoonfar et al. (2021). These capabilities are enabled by a growing fleet of EO satellites, most notably the Sentinel missions, which deliver multi-modal, multi-temporal data at a global scale Torres et al. (2012); Drusch et al. (2012). The rise of deep learning, particularly deep neural networks (DNNs), has fundamentally reshaped the way EO data is processed and interpreted Wang et al. (2025); Szwarcman et al. (2024); Tseng et al. (2025). Modern DNNs enable automated extraction of spatial and semantic patterns from raw imagery, driving downstream tasks such as scene classification, object detection, and semantic segmentation Astruc et al. (2024); Waldmann et al. (2025); Kuckreja et al. (2024); Tseng et al. (2025); Fuller et al. (2023). These models offer a scalable alternative to traditional hand-engineered pipelines by learning generalizable representations directly from data Guo et al. (2024). As EO data continue to expand in scale, diversity, and complexity, DNNs have become foundation for building high-capacity models capable of generalizing across geographies, modalities, and tasks Szwarcman et al. (2024); Astruc et al. (2024); Waldmann et al. (2025).

Remote sensing data is inherently multimodal, comprising diverse sensor types such as optical, SAR, and multispectral imagery. Traditional EO pipelines often focus on single-modality inputs, typically high-resolution optical imagery, limiting the model's ability to generalize across varying sensing conditions. In contrast, multimodal and multispectral data sources, such as Sentinel-1 SAR and Sentinel-2 Level-1C/Level-2A optical bands, capture complementary structural and spectral information, enabling richer scene understanding Han et al. (2024); Fuller et al. (2023). Foundation models that embrace this diversity have demonstrated superior transferability across tasks and geographies Tseng et al. (2025); Guo et al. (2024). However, variation in ground sampling distance (GSD) across EO data makes tile size a critical factor; smaller tiles capture local detail but risk overfitting to texture, while larger tiles provide broader semantic context but require scale-robust architectures Reed et al. (2023). Recent works like AnySat Astruc et al. (2024) and msGFM Han et al. (2024); Astruc et al. (2024) have shown that scale-invariant modeling and mixed-resolution pretraining lead to more robust and generalizable representations. Crucially, large-scale sampling across geographies and resolutions enables EO foundation models to learn invariant features across sensors and global conditions.

As EO foundation models scale to accommodate diverse sensor inputs and resolutions, two dominant pretraining paradigms have emerged: masked autoencoders (MAE) and contrastive learning. Although MAEs focus on reconstructing the spatial structure, their reliance on RGB-centric ViTs limits their adaptability to multispectral or SAR inputs with varying spectral dimensions Li et al. (2024); Szwarcman et al. (2024). In contrast, contrastive approaches such as DINO Caron et al. (2021); Oquab et al. (2023) and its adaptations to remote sensing Tseng et al. (2025); Fuller et al. (2023); Waldmann et al. (2025) offer modality-agnostic training by aligning global and local views through student-teacher distillation. However, the expansive spatial coverage of EO datasets introduces new challenges: large portions of satellite imagery are semantically sparse or uninformative, and naïve sampling can lead to representation bias. This requires intelligent sampling that prioritizes semantically diverse regions, guided by land cover priors, for balanced and efficient representation learning.

To address these limitations in standard ViTs, particularly their RGB-centric design, lack of modality awareness, and unimodal self-supervision, we introduce **TerraFM**, a unified foundation model tailored for remote sensing. First, we propose a *Modality-Specific Patch Embedding* module, which replaces the shared projection in standard ViTs with modality-aware embeddings adapted to multispectral and SAR data. This enables flexible handling of sensor-specific spectral profiles while preserving spatial structure. To enhance scale-invariance and cross-view consistency, we adopt multi-crop learning within a self-supervised teacher-student framework, promoting robust representation learning through global-local alignment. Further, we interpret different aligned modalities (S1-SAR, S2-L1C, S2-L2A) as complementary views of the same scene and introduce a *Cross-Attention Fusion* module that dynamically aggregates modality-specific tokens using learnable spatial queries. This allows the model to selectively emphasize sensor contributions at each spatial location. Finally, to mitigate long-tailed land cover distribution issues prevalent in EO data, we introduce a *Dual Centering* mechanism into the distillation process. This leverages WorldCover Zanaga et al. (2022) derived class statistics to compute a frequency-aware center, improving balance across dominant and rare semantic categories without requiring supervised objectives. These challenges highlight the need for a unified multimodal framework that scales effectively across sensors and resolutions. Our approach, TerraFM, directly addresses these issues as shown in Fig. 1, achieves superior performance compared to recent EO foundation models. Our key contributions are:

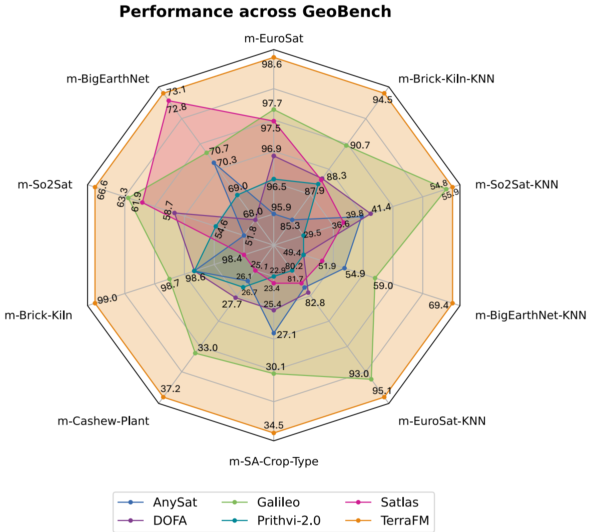

Figure 1: Performance comparison across GEO-Bench classification tasks using supervised fine-tuning and kNN evaluation. Five recent EO foundation models: AnySat Astruc et al. (2024), DOFA Xiong et al. (2024), Galileo Tseng et al. (2025), Prithvi-2.0 Szwarcman et al. (2024), and Satlas Bastani et al. (2023) are compared against our TerraFM, which consistently outperforms them across modalities and evaluation settings, demonstrating strong generalization.

Contributions: **(1)** A *modality-specific patch embedding* mechanism is introduced to generalize ViTs across heterogeneous remote sensing modalities with varying spectral dimensions. **(2)** We treat sensor modalities as natural augmentations and introduce a *cross-attention fusion* block that unifies multi-modal inputs within a shared encoder. **(3)** To address long-tailed LULC distributions, a *dual-centering* strategy is incorporated to regularize representation learning using class-frequency-aware statistics. **(4)** Extensive experiments on *GEO-Bench* and *Copernicus-Bench* demonstrate leading performance across multiple downstream tasks using globally distributed data.

2 RELATED WORK

Self-supervised Pretraining: MAEs He et al. (2022) have become a popular choice for self-supervised pretraining in remote sensing by reconstructing masked image regions using ViT Dosovitskiy et al. (2021). Variants like Scale-MAE Reed et al. (2023) and MC-MAE Gao et al. (2022) enhance robustness across spatial scales via scale-aware encodings and convolutional tokenizers. However, MAEs struggle to scale to multisensor EO data, as their RGB-centric tokenization and reconstruction objectives limit generalization to multispectral and SAR modalities with diverse channel structures Xie et al. (2023); Li et al. (2024).

Unlike MAEs, self-supervised contrastive learning focuses on learning discriminative representations by comparing semantically similar and dissimilar views. Remote sensing approaches Tang et al. (2023); Fuller et al. (2023); Waldmann et al. (2025) leverage spatial and spectral augmentations to create diverse yet consistent views. CROMA Fuller et al.

Table 1: Comparison of recent remote sensing foundation models across modalities, scale, and benchmarks. **TerraFM** uniquely blends large tile size, WorldCover-informed metadata, and global-scale training (18.7M samples) with evaluation on both GEO-Bench and Copernicus-Bench.

Model	**Modalities**	**Scale**	**Resolution**	**TileSize**	**Metadata**	**Benchmarks**	**Pixels (~T)**
SatMAE++	S2, RGB	$\sim$1.2 M	10–60 m	224, 96	No	6 DS	0.12
Galileo	S1, S2, NDVI, ESA WC etc	$\sim$3–10.9 M	10 m	96 (flex)	Yes	GEO + 5 DS	1.58
CROMA	S1, S2	$\sim$1 M	10 m	96, 120	No	7 DS	0.98
SoftCon	S1, S2	$\sim$0.78 M	10 m	224	Yes	4 GEO + 7 DS	0.76
AnySat	Aerial, S1/S2, MODIS, etc.	11.1 M	0.2–250 m	10–240	No	11 DS	0.17
Prithvi-2	S2, HLS	4.2 M	30 m	224	Yes	GEO + 9 SME	5.06
DOFA	S1, S2, EnMAP, etc.	$\sim$8 M	1–30 m	512, 128	Yes	GEO + 2 DS	6.74
Panopticon	S1, S2, WV2/3, NAIP	$\sim$2.6 M	0.3–100 m	96, 224	Yes	GEO + 10 DS	2.34
MMEarth	S1, S2, DEM, etc.	$\sim$7.2 M	0.3–100 m	128	Yes	5 GEO	0.51
msGFM	RGB, S2, SAR, DSM	$\sim$2 M	0.1–30 m	192	No	5 DS	0.44
Copernicus-FM	S1–S5P, DEM	18.7 M	10 m–1 km	Mixed	Yes	Cop-Bench	5.12
TerraFM (Ours)	S1, S2 L1C/L2A	18.7 M	10–60 m	534	Yes	GEO + Cop-Bench	**23.32**

(2023) combines contrastive and masked autoencoding losses, while Cross-Scale MAE Tang et al. (2023) blends generative and contrastive objectives for multi-scale learning. Student-teacher frameworks like DINO Caron et al. (2021); Oquab et al. (2023) scale contrastive learning via EMA-updated teachers and global-local view alignment with centering to prevent collapse. These strategies are well-suited for EO, where multimodal imagery can act as natural augmentations, enabling scalable, label-free training and broad generalization.

Remote Sensing FMs: Recent advances in remote sensing foundation models (FMs) have scaled self-supervised learning across architecture types, modalities, training sizes, tile resolutions, and metadata usage (Table 1). Multimodal integration is central to recent FMs like Guo et al. (2024); Wang et al. (2025); Waldmann et al. (2025); Astruc et al. (2024); Tseng et al. (2025); Han et al. (2024). SkySense Guo et al. (2024) applies contrastive learning to temporal-multimodal data but requires large-scale compute. CopernicusFM Wang et al. (2025) fuses Sentinel modalities via metadata-aware networks but faces scaling issues with heterogeneous inputs. Panopticon Waldmann et al. (2025) and AnySat Astruc et al. (2024) align cross-modal views through contrastive training, while Galileo Tseng et al. (2025) uses shared embeddings for SAR and multispectral fusion. Fus-MAE Chan-To-Hing & Veeravalli (2024) adopts attention-based fusion without contrastive loss, limiting generalization.

Prithvi-2 Szwarcman et al. (2024) is restricted to single-modal optical data with temporal-spatial modeling. DOFA Xiong et al. (2024), msGFM Han et al. (2024), and AnySat Astruc et al. (2024) address resolution variability using mixed tile sizes or scale-adaptive designs. Our 534px tiles capture broader spatial context than prior RSFMs. While CopernicusFM Wang et al. (2025) and DOFA Xiong et al. (2024) incorporate metadata, we leverage land cover (LULC) priors for semantically informed learning. Both CopernicusFM and our model are trained on 18.7M samples, but ours uses over 23T pixels during pretraining, scaling the 5.1T used by Copernicus-Pretrain Wang et al. (2025) over 4x. This growing body of work makes clear that the next step is moving beyond single-modality or scale-limited pipelines toward unified, globally robust EO foundation models.

3 TERRAFM: A SCALABLE MULTISENSOR FOUNDATIONAL MODEL

Unlike prior remote sensing foundation models, our approach integrates a student–teacher contrastive learning framework with dual centering (to balance long-tailed classes), modality-as-augmentation (to learn cross-modal invariances), and cross-attention fusion (to aggregate multi-sensor context), as illustrated in Figure 2. Built on a ViT backbone and trained on 18.7M globally distributed samples using 534×534 tiles, **TerraFM** captures broader spatial context and generalizes effectively across sensing modalities and geographies, achieving strong results on diverse downstream benchmarks.

3.1 ARCHITECTURE

We use globally distributed remote sensing imagery organized over a spatial grid, partitioning the earth's surface into fixed-size tiles Francis & Czerkawski (2024). Each spatial unit, denoted as s, represents one such grid cell. For each sample, we observe a set of co-registered EO modalities:

$$\mathcal{M} = \{\text{S1},\ \text{S2-L1C},\ \text{S2-L2A}\},$$

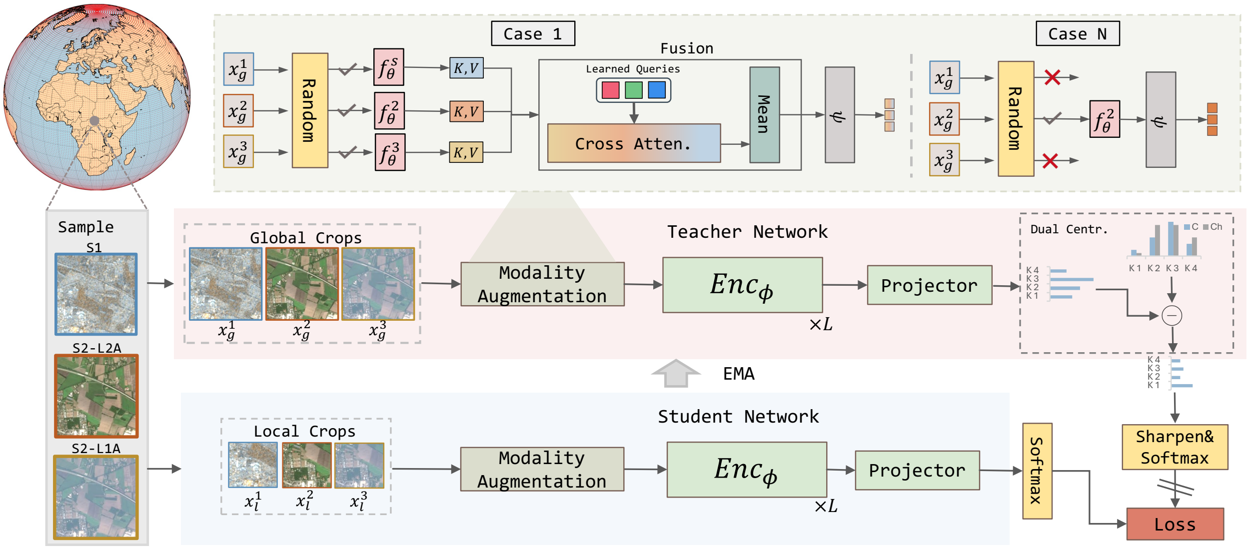

Figure 2: Overall architecture of **TerraFM**. It unifies student-teacher contrastive framework with modality augmentation with cross-attention fusion, and a new dual centering regularization. **TerraFM** is founded on ViT backbone and is trained on 18.7M globally distributed samples for pre-training and utilizes large-tile inputs for encoding broader spatial context. For *illustration*, RGB channels from S2-L2A and S2-L1C are selected, and S1 is visualized using a false-color RGB composite.

where **S1** corresponds to Sentinel-1 SAR, and **S2-L1C** and **S2-L2A** represent two processing levels of Sentinel-2 optical imagery: Level-1C (top-of-atmosphere reflectance) and Level-2A (bottom-of-atmosphere surface reflectance), respectively. Each modality $m \in \mathcal{M}$ provides a multi-channel image $\boldsymbol{x}^m \in \mathbb{R}^{H\times W\times C_m}$, where H and W denote spatial dimensions, and C_m is the number of spectral channels for modality m. For example, Sentinel-1 contains two channels (VV and VH polarizations), therefore $C_{\text{S1}} = 2$, while Sentinel-2 modalities contain up to 13 spectral bands depending on level and resolution. These modalities are treated as complementary views of the same location, acting as natural augmentations, which support our training strategy and encourage learning modality-invariant representations. To provide semantic grounding, each sample s is assigned a high-level land use and land cover (LULC) category $y^{(s)} \in \{1, \ldots, Y\}$, derived from the ESA WorldCover product. These categories reflect coarse semantic classes at a global scale and are used to compute class-frequency-aware statistics for balanced representation learning.

Vision Transformer Model: ViTs adapt the transformer architecture to visual data by treating an image as a sequence of patch tokens instead of a dense pixel grid. A typical ViT consists of two main components: a patch embedding module and a transformer encoder. Given an input image $\boldsymbol{x} \in \mathbb{R}^{H\times W\times C}$, the **patch embedding** layer f_θ divides the image into N non-overlapping patches of size $P \times P$, and projects each patch into a d dimensional embedding:

$$\{\boldsymbol{z}_i\}_{i=1}^N = f_\theta(\boldsymbol{x}), \qquad \boldsymbol{z}_i \in \mathbb{R}^d.$$

This projection is typically implemented using a convolutional layer with kernel size and stride equal to the patch size P, parameterized by weights $\mathbf{W}_\theta \in \mathbb{R}^{d\times C\times P\times P}$. To encode spatial information, the transformer encoder augments each patch token $\boldsymbol{z}_i$ with a positional vector. A learnable class token $\boldsymbol{z}_{\text{cls}}$ is added to the sequence, which yields the full input:

$$\boldsymbol{Z} = \left[\, \boldsymbol{z}_{\text{cls}};\ \{\boldsymbol{z}_i + \text{pos}_i\}_{i=1}^N \,\right].$$

The token sequence $\boldsymbol{Z}$ is processed by a stack of L transformer layers, denoted Enc_ϕ. For classification tasks, only the final class token $\boldsymbol{z}_{\text{cls}}$ is forwarded to a prediction head.

Modality-Specific Patch Embedding: Standard patch embedding layers in ViTs are typically implemented using a shared convolutional projection across all inputs, making it unsuitable for multi-modal remote sensing data. To better handle this heterogeneity, we adopt a modality-specific patch embedding strategy. For each modality $m \in \mathcal{M}$, we define an embedding function f_{θ_m} that maps the input image $\boldsymbol{x}^{(m)} \in \mathbb{R}^{H\times W\times C_m}$ to a sequence of patch tokens $\bar{\boldsymbol{Z}}^{(m)} \in \mathbb{R}^{N\times D}$, where C_m is the number of channels and N is the number of patches. Each f_{θ_m} is parameterized independently to account for modality-specific dynamics. We associate each modality with a learnable embedding vector $\boldsymbol{\epsilon}^{(m)} \in \mathbb{R}^D$. This vector is added to every token from that modality via broadcasting:

$$\tilde{\boldsymbol{Z}}^{(m)} = \bar{\boldsymbol{Z}} + \mathbf{1}_N \cdot (\boldsymbol{\epsilon}^{(m)})^\top,$$

where $\mathbf{1}_N \in \mathbb{R}^{N\times 1}$ is a vector of ones. This allows the model to distinguish between modalities while preserving local spatial and spectral features. Finally, to enable shared processing in the Transformer encoder, the enriched tokens $\tilde{\boldsymbol{Z}}^{(m)}$ are linearly projected into a common latent space of dimension d using a shared projection $\psi : \mathbb{R}^D \to \mathbb{R}^d$:

$$\boldsymbol{Z}^{(m)} = \psi(\tilde{\boldsymbol{Z}}^{(m)}) \in \mathbb{R}^{N\times d}.$$

This operation aligns all modality-specific token sequences in a unified representation space, allowing the encoder to process them jointly.

Modality Augmentation and Cross-Attention Fusion: Remote sensing observations of a single location are often captured using multiple sensors, each providing a unique spectral or radiometric perspective. Instead of treating these modalities as independent inputs, we interpret them as complementary views of the same scene. This allows us to use modality diversity as a form of natural augmentation, enabling the model to learn sensor-invariant representations. In our setup, each spatial sample s from the Major-TOM dataset Francis & Czerkawski (2024) is observed via a fixed set of modalities. During pretraining, we independently assign modalities to the student and teacher networks via stochastic selection (threshold = 0.5), ensuring cross-modal supervision. E.g., the teacher may observe a global crop from Sentinel-1, while the student receives local views from Sentinel-2 L2A. This modality augmentation strategy encourages the model to align features across sensors, improving robustness to sensor-specific artifacts. We consider two cases based on the number of selected modalities:

1) Single-Modality Views: If only one modality is selected, the input is passed through the corresponding modality-specific patch embedding layer followed by the shared transformer encoder. This follows the standard ViT pipeline but uses modality-aware embeddings to handle spectral channel differences. **2) Multi-Modality Fusion via Cross-Attention:** When multiple modalities $M \subseteq \mathcal{M}$ are selected, we activate a modality fusion module based on cross-attention. For each selected modality $m \in M$, we obtain a patch token sequence $\bar{\boldsymbol{Z}}^{(m)} \in \mathbb{R}^{N\times D}$, where N is the number of spatial positions. These are stacked into a tensor $\boldsymbol{Z}_{\text{all}} \in \mathbb{R}^{N\times M\times D}$, aligning spatial positions across modalities. For each position $n = 1, \ldots, N$, we define shared learnable queries $\boldsymbol{q} \in \mathbb{R}^{N_q\times D}$, which attend to modality-specific keys $\boldsymbol{K}_n \in \mathbb{R}^{M\times D}$ and values $\boldsymbol{V}_n \in \mathbb{R}^{M\times D}$, yielding N_q intermediate outputs:

$$\boldsymbol{z}'_n = \texttt{MultiHeadAttention}(\boldsymbol{q}, \boldsymbol{K}_n, \boldsymbol{V}_n) \in \mathbb{R}^{N_q\times D}.$$

To aggregate them, we compute a learned weighted mean using softmax-normalized attention scores:

$$\boldsymbol{w} = \texttt{Softmax}(\boldsymbol{z}'_n \cdot \boldsymbol{p}_r), \quad \boldsymbol{z}_n^{\text{fused}} = \sum_{j=1}^{N_q} w_j \boldsymbol{z}'_n[j],$$

where $\boldsymbol{p}_r \in \mathbb{R}^{D\times 1}$ is a learnable projection for scoring the query outputs. This results in a fused token $\boldsymbol{z}_n^{\text{fused}} \in \mathbb{R}^D$. The final sequence $\boldsymbol{Z}_{\text{fused}} \in \mathbb{R}^{N\times D}$ is then passed to the shared encoder Enc_ϕ. This cross-attention fusion allows the model to dynamically weigh the modality contributions at each spatial location, capturing diverse information while maintaining spatial coherence.

3.2 PRETRAINING

Our pretraining strategy builds on the DINO framework, which performs self-supervised learning. It operates using a teacher-student setup, where both networks share the same ViT backbone and a lightweight three-layer projection head. Let g_{θ_s} and g_{θ_t} denote the student and teacher networks, respectively. While the student is trained using gradient-based optimization, the teacher is updated using EMA of the student's weights:

$$\theta_t \;\leftarrow\; \lambda_e\, \theta_t + (1-\lambda_e)\, \theta_s, \quad \lambda_e = 1 - (1-\lambda_0)\frac{1+\cos(\pi e/E)}{2}, \tag{1}$$

where e is the current epoch, E is the total number of training epochs, and $\lambda_0 \in [0.996, 1)$ is the initial momentum coefficient. The cosine schedule gradually increases λ_e, stabilizing the teacher updates as training progresses. This EMA mechanism allows the teacher to serve as a temporally smoothed ensemble of past student states, yielding more stable and consistent targets.

Multi-Crop Learning: To enable scale-invariant and cross-view representation learning, we adopt a multi-crop strategy as used in DINO Caron et al. (2021). For each input sample, we generate two high-resolution global crops $\{\boldsymbol{x}_g^{(1)}, \boldsymbol{x}_g^{(2)}\} \subset \mathcal{X}_g$ and J low-resolution local crops $\{\boldsymbol{x}_\ell^{(j)}\}_{j=1}^J \subset \mathcal{X}_\ell$. The teacher network processes only the global crops, while the student receives both global and local views. Each network produces a K-dim output which is temperature-scaled and normalized via the softmax function:

$$Q_s^{(i)}(\boldsymbol{x}) = \frac{\exp(g_{\theta_s}(\boldsymbol{x})^{(i)}/\tau_s)}{\sum_{k=1}^K \exp(g_{\theta_s}(\boldsymbol{x})^{(k)}/\tau_s)}, \quad Q_t^{(i)}(\boldsymbol{x}) = \frac{\exp((g_{\theta_t}(\boldsymbol{x})^{(i)} - c^{(i)})/\tau_t)}{\sum_{k=1}^K \exp((g_{\theta_t}(\boldsymbol{x})^{(k)} - c^{(k)})/\tau_t)},$$

where τ_s and τ_t are temperature parameters that control output sharpness, and $c \in \mathbb{R}^K$ is a centering term representing the running mean of teacher logits, used to stabilize training and avoid representation collapse. The centering term is updated using an exponential moving average over the teacher outputs:

$$c \leftarrow \beta c + (1 - \beta) \cdot \frac{1}{B} \sum_{i=1}^{B} g_{\theta_t}(\boldsymbol{x}_i),$$

where $\beta \in [0.9, 0.999]$ controls the momentum, and B is the batch size. The overall loss encourages consistency between teacher and student predictions across all distinct view pairs:

$$\sum_{\boldsymbol{x} \in \mathcal{X}_g} \sum_{\boldsymbol{x}' \in \mathcal{X}; \boldsymbol{x}' \neq \boldsymbol{x}} \mathcal{L}_{\text{CE}} \left(Q_t(\boldsymbol{x}), Q_s(\boldsymbol{x}') \right),$$

where $\mathcal{X} = \mathcal{X}_g \cup \mathcal{X}_\ell$, and $\mathcal{L}_{\text{CE}}(\cdot, \cdot)$ denotes the cross-entropy loss. This loss formulation requires the student to produce consistent representations in all views.

Dual Centering for Long-Tailed Distributions:

Remote sensing datasets often exhibit long-tailed distributions of LULC classes, with frequent categories such as Forest dominating, while classes like Urban or Bare Land remain underrepresented as shown in Figure 3. This imbalance persists even after subsampling and poses challenges for representation learning. Standard self-supervised approaches like DINO Caron et al. (2021) apply a single global centering term to stabilize training and avoid representation collapse, but they do not account for semantic imbalance in the data. To address this, we propose a dual-centering scheme that combines global statistics with class-frequency-aware regularization. In addition to the standard global center vector c, we introduce a secondary center $c_h \in \mathbb{R}^K$, computed from a subset of samples belonging to high-frequency LULC classes, such as tree cover, grassland, and open seas, based on dataset-level statistics. Given a batch of teacher logits $g_{\theta_t}(\boldsymbol{x})$, the adjusted logits for training are computed as:

$$\hat{g}(\boldsymbol{x}) = g_{\theta_t}(\boldsymbol{x}) - \alpha \cdot c - (1 - \alpha) \cdot c_h,$$

where $\alpha \in [0, 1]$ balances the contribution of the global and frequency-aware centers. The vector c_h is updated via exponential moving average using only frequent-class samples within each batch. This dual-centering mechanism serves two key purposes: **(i)** it preserves the stability benefits of global centering as in DINO, and **(ii)** it introduces a soft rebalancing bias that counteracts the overrepresentation of dominant classes in the feature space. In ablations (Table 5), this adjustment leads to more balanced representation learning and improved downstream performance, particularly for underrepresented LULC categories.

4 PRETRAINING DATA SAMPLING

We utilize the Major-TOM dataset Francis & Czerkawski (2024) as our primary EO source for pertaining. It contains 2.24 million globally distributed grid cells, each spanning approximately 10.68 km × 10.68 km ($\approx$114 km^2), and provides tri-modal, co-registered imagery from Sentinel-2 Level-1C, Sentinel-2 Level-2A, and Sentinel-1 RTC. Major-TOM stands out as one of the few publicly available datasets offering dense multi-modal coverage at a global scale. However, over one-third of its samples lie outside a 10 km terrestrial buffer, often within the Open Oceans class Zanaga et al. (2022), limiting their relevance for land-centric tasks. Motivated by insights from Roscher et al. (2024), which emphasize the importance of semantically rich samples, and Wang et al. (2024d), which highlight the utility of structural priors, we applied a principled filtering strategy. Specifically, we removed 98% of ocean-classified tiles (retaining 2% to preserve marine representation) and sampled the terrestrial subset using global distributional priors across land cover Zanaga et al. (2022), climate zones Beck et al. (2018), and ESRI world regions Esri et al. (2025). This approach emphasizes meaningful land regions with ecological variety. Figure 3 shows the global coverage of the tile and Figure Ap4 in the Appendix covers the map. For pretraining, we curated a filtered subset of over 1.5 million grid cells with consistent coverage across all three modalities (S1, S2-L1C, and S2-L2A). Each 10.68 km × 10.68 km grid cell was divided into four non-overlapping tiles of 534 × 534 pixels, resulting in more than 6

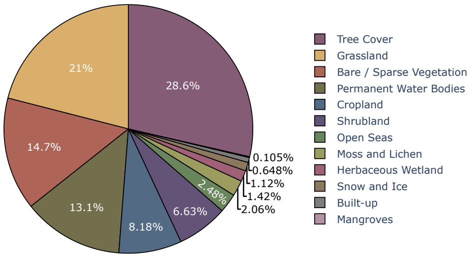

Figure 3: Land-use/land-cover (LULC) breakdown across the training tiles. A number of semantically important classes (e.g., builtup, mangroves, ice) remain underrepresented due to skewed data distribution.

million tiles per modality. In total, this yielded 18.7 million modality-specific training tiles. During training, modalities were stochastically sampled and treated as natural augmentations to promote sensor-invariant representation learning. To mitigate spatial sampling bias and support semantically-aware learning, we enriched each grid cell with metadata from the ESRI World Regions dataset Esri et al. (2025).

5 EXPERIMENTS AND RESULTS

5.1 PRETRAINING IMPLEMENTATION DETAILS

We pre-train TerraFM using 534×534 tiles as inputs. Following the DINO-style cropping strategy Caron et al. (2021), each tile is randomly cropped at two scales: (i) *global crops*, sampled with ratios in $[0.25, 1.0]$ of the tile size and resized to 224×224, and (ii) *local crops*, sampled with ratios in $[0.05, 0.25]$ and resized to 96×96. All inputs are then tokenized with a 16×16 patch resolution. The training dataset comprises around 1.53 million multi-modal samples, from which we define a virtual epoch of 300K samples to ensure frequent parameter updates. TerraFM-B is trained for 150 epochs and TerraFM-L for 200 epochs, each with a linear warmup over the first 30 epochs. Models are trained on 64 GPUs, TerraFM-B training takes 92 hours with a batch size of 1024, while TerraFM-L uses a batch size of 2048 and trains for 183 hours. The learning rate is linearly scaled with batch size, initialized as $\text{lr} = 0.0001 \times \text{batch\_size}/256$. Following DINO-style pretraining, we disable batch normalization in the projection head and freeze the last layer of the student for the first 3 epochs to stabilize early training. The output dimensionality is set to $K = 65{,}536$, with the teacher temperature linearly increasing from 0.04 to 0.06 over the first 50 epochs. The teacher momentum follows a cosine schedule starting from 0.996. A drop path rate of 0.1 is applied for regularization. For modality fusion, we set $N_q = 5$ and $\alpha = 0.8$ during pretraining.

5.2 EVALUATING DOWNSTREAM TASKS

Benchmarks: We evaluate our model on two comprehensive remote sensing benchmarks: **GEO-Bench** Lacoste et al. (2023) and **Copernicus-Bench** Wang et al. (2024a), both of which include diverse downstream tasks spanning multiple domains and modalities. The benchmark datasets are described in Appendix A, and for evaluation protocols (linear probing, UperNet probing, k-NN, and fine-tuning), we refer the reader to Appendix C.1.

Discussion: We report KNN classification accuracy on four standard GEO-Bench classification tasks to evaluate the quality of learned representations in a training-free setting. As shown in Table 2, TerraFM achieves the highest performance across three datasets, outperforming both modality-specific and multimodal foundation models. Notably, our model achieves 95.1% on m-EuroSAT and 94.5% on m-Brick-Kiln, highlighting the effectiveness of the learned representations on standard scene classification tasks. On other challenging tasks such as m-So2Sat and m-BigEarthNet, our model achieves leading performance (55.9% and 69.4%, respectively), outperforming Galileo Tseng et al. (2025), despite So2Sat having fewer channels than used during pretraining, highlighting the model's robustness to missing modality information. Compared to CROMA Fuller et al. (2023) and DeCUR Wang et al. (2024a), our gains suggest that contrastive alignment combined with cross-modal fusion enhances class separability. The results across tasks of

Table 2: We evaluate image classification using k-nearest neighbors (kNN) and report Top-1 accuracy for all single-label tasks. For the multilabel BigEarthNet benchmark, we report the F1 score. Results other than Copernicus-FM and TerraFM are directly taken from Tseng et al. (2025).

		m-EuroSat Training %		m-BigEarthNet Training %		m-So2Sat Training %		m-Brick-Kiln Training %	
Model	Backbone	100%	1%	100%	1%	100%	1%	100%	1%
SatMAE (Cong et al. (2022))	ViT-Base	84.1	34.8	50.6	29.0	36.0	23.1	86.1	73.5
SatMAE++ (Noman et al. (2024))	ViT-Large	82.7	48.5	50.8	31.6	34.7	23.4	89.6	76.7
CROMA (Fuller et al. (2023))	ViT-Base	85.6	51.3	58.8	44.7	48.8	33.8	92.6	85.1
SoftCon (Wang et al. (2024b))	ViT-Small	89.8	27.2	64.7	43.3	51.1	31.4	89.2	77.8
DOFA (Xiong et al. (2024))	ViT-Base	82.8	49.6	49.4	29.9	41.4	29.4	88.3	78.3
Satlas (Bastani et al. (2023))	Swin-Tiny	81.7	35.8	51.9	29.6	36.6	27.1	88.2	73.0
MMEarth (Nedungadi et al. (2024))	CNN-atto	81.7	30.0	58.3	39.6	39.8	25.1	89.4	79.7
DeCUR (Wang et al. (2024a))	ViT-Small	89.0	46.6	63.8	49.6	45.8	30.9	83.7	74.2
AnySat (Astruc et al. (2024))	ViT-Base	82.2	47.1	54.9	33.7	39.8	29.0	85.3	72.0
Galileo (Tseng et al. (2025))	ViT-Base	93.0	56.6	59.0	36.5	54.8	**43.2**	90.7	78.0
Prithvi-2.0 (Szwarcman et al. (2024))	ViT-Large	80.2	48.0	49.4	28.8	29.5	26.1	87.9	80.6
Copernicus-FMWang et al. (2025)	ViT-Base	76.0	47.4	53.8	33.3	38.4	23.3	93.0	83.2
TerraFM (Ours)	ViT-Base	94.2	59.3	68.7	49.4	55.1	41.6	**94.5**	**85.6**
	ViT-Large	**95.1**	**62.1**	**69.4**	**50.6**	**55.9**	41.1	93.0	82.2

Table 3: Performance comparison on GEO-Bench for both classification (Top-1 Accuracy), segmentation (mIoU), and F1 score (for m-BigEarthNet). TerraFM achieves state-of-the-art results across multiple datasets, outperforming previous FMs.

		Classification				**Segmentation**	
Method	Backbone	m-EuroSat	m-BigEarthNet	m-So2Sat	m-Brick-Kiln	m-Cashew-Plant	m-SA-Crop-Type
SatMAE	ViT-Large	96.6	68.3	57.2	98.4	30.8	24.8
SatMAE++	ViT-Large	96.5	67.9	56.0	98.6	29.6	25.7
CROMA	ViT-Large	96.6	71.9	60.6	98.7	31.8	32.0
SoftCon	ViT-Base	97.5	70.3	61.7	98.7	29.6	30.8
DOFA	ViT-Large	96.9	68.0	58.7	98.6	27.7	25.4
Satlas	Swin-Base	97.5	72.8	61.9	98.4	25.1	23.4
MMEarth	CNN-atto	95.7	70.0	57.2	98.9	24.2	22.2
DeCUR	ViT-Small	97.9	70.9	61.7	98.7	26.2	21.5
Prithvi 2.0	ViT-Large	96.5	69.0	54.6	98.6	26.7	22.9
AnySat	ViT-Base	95.9	70.3	51.8	98.6	26.1	27.1
Galileo	ViT-Base	97.7	70.7	63.3	98.7	33.0	30.1
TerraFM	ViT-Base	98.1	72.6	64.9	98.7	34.1	33.0
	ViT-Large	**98.6**	**73.1**	**66.6**	**99.0**	**37.2**	**34.5**

varying difficulty indicate that our model learns robust and transferable representations that generalize well across different scenarios.

Further GEO-Bench results with fine-tuning and linear probing are reported in Table 3, for classification (with fine-tuning), TerraFM achieves the improvement on m-BigEarthNet (73.1%) and m-EuroSat (98.6%), and the best-performing model on m-So2Sat (66.6%). For segmentation (with linear probing), our TerraFM-L notably outperforms existing models on m-SA-Crop-Type (34.5% mIoU) and m-Cashew-Plant (37.2% mIoU). TerraFM-B surpasses larger counterparts such as ViT-Large used in SatMAE++Noman et al. (2024) and DOFAXiong et al. (2024). On the Copernicus-Bench Wang et al. (2025) (Table 4), TerraFM delivers state-of-the-art results across most tasks and modalities. It achieves 67.9 mIoU on Cloud-S2, 87.8 OA on EuroSAT-S1, and 99.1 OA on EuroSAT-S2, surpassing all prior models. On BigEarthNet-S2 and DFC2020-S1, TerraFM attains 84.4 mAP and 55.4 mIoU, respectively, marking clear gains over existing FMs. While SoftCon Wang et al. (2024b) is slightly higher on BigEarthNet-S1 (78.7 vs. 76.9), TerraFM consistently outperforms Copernicus-FM Wang et al. (2025) despite sharing the same ViT-B/16 backbone. These results highlight TerraFM's scalability and strong generalization across diverse EO benchmarks.

Table 4: Comparison of TerraFM with supervised and self-supervised methods on Copernicus-Bench. Metrics: OA (Overall Accuracy for classification), mAP (mean Average Precision for multi-label classification), mIoU (mean Intersection over Union for segmentation). Baselines include SoftCon Wang et al. (2024b), CROMA Fuller et al. (2023), DOFA Xiong et al. (2024), and Copernicus-FM Wang et al. (2025).

Model / Metric	**Cloud-S2 (mIoU)**	**EuroSAT-S1 (OA)**	**EuroSAT-S2 (OA)**	**BigEarthNet-S1 (mAP)**	**BigEarthNet-S2 (mAP)**	**DFC2020-S1 (mIoU)**	**DFC2020-S2 (mIoU)**	**LCZ-S2 (OA)**
Supervised (ViT-B/16)	59.4	81.5	97.6	70.6	80.1	50.8	66.2	85.3
Random (ViT-B/16)	60.4	75.4	92.5	63.8	71.6	45.4	62.3	77.4
SoftCon (ViT-B/14)	66.9	83.6	96.7	**78.7**	83.6	52.8	64.1	83.6
CROMA (ViT-B/8)	65.0	83.9	97.0	70.8	76.4	52.7	**66.5**	84.1
DOFA (ViT-B/16)	65.0	81.7	97.2	70.5	75.5	49.7	61.8	83.0
Copernicus-FM (ViT-B/16)	66.7	87.2	97.9	77.9	79.0	52.4	64.5	84.4
TerraFM (ViT-B/16)	**67.9**	**87.8**	**99.1**	76.9	**84.4**	**55.4**	63.8	**87.0**

5.3 ABLATIONS AND ANALYSIS

Impact of Components: Table 5 highlights the incremental benefits of each component in our framework. We train TerraFM-B for 150 epochs on a 200k-sample subset from our full training dataset. The model was trained on a subset of the training data, and KNN classification accuracy is reported for each dataset. To measure the performance on segmentation task, we use uppernet probing on the m-Cashew-Plantation dataset from GeoBench. Adding modality as augmentation improves performance on m-EuroSat by +4.5% and m-BigEarthNet by +3.01%. Incorporating fusion yields a large gain on m-Cashew-Plantation by +11.82%, while dual centering provides further improvements: +3.44% on m-BigEarthNet, +7.2% on m-EuroSat, and +14.0% on m-Cashew-Plantation.

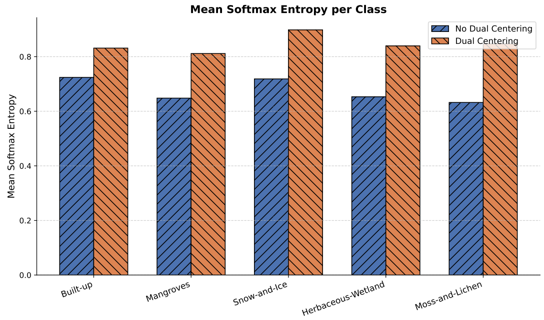

Figure 4: Mean entropy per LULC class from 5k training samples, with logits ($K = 65{,}536$) reduced via Gaussian projection. The baseline (no dual-centering) shows lower entropy and overconfident predictions skewed to frequent classes. Dual-centering increases entropy, yielding more balanced predictions, especially for rare classes like Mangroves and Herbaceous-Wetland.

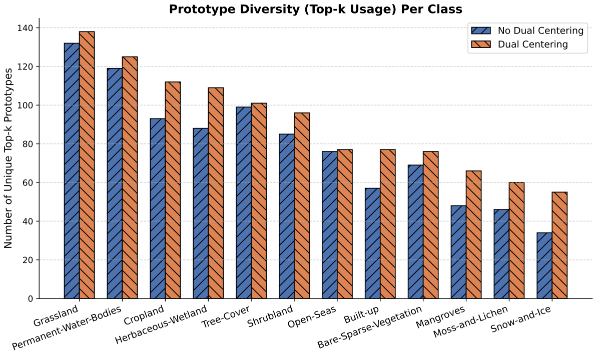

Figure 5: Prototype diversity is measured as the number of unique top-5 prototypes across 5k training samples. Dual-centering improves diversity for tail classes like Mangroves, Herbaceous-Wetland, and Built-up, indicating richer representations. The baseline reuses fewer prototypes, reflecting over-reliance on dominant frequent-class features.

SS	MAug	Fus	DC	BEN	ES	CP
✓	–	–	–	54.62	83.20	50.58
✓	✓	–	–	57.63	87.70	59.17
✓	✓	✓	–	57.74	88.50	62.40
✓	✓	✓	✓	58.06	90.40	64.58

Table 5: Ablation of components: SS = Self-supervised contrastive learning, MAug = Modality Augmentation, Fus = Fusion, DC = Dual Centering. BEN = m-BigEarthNet, ES = m-EuroSat, CP = m-Cashew-Plant.

Dual-centering Motivation and Visualization: Here, we discuss the impact of Dual-centering on class-wise prediction behavior and representation diversity. Figure 4 shows that models with Dual-centering exhibit higher softmax entropy across most classes, indicating more calibrated predictions, particularly benefiting rare classes like "Mangroves". Figure 5 reveals that Dual Centering significantly increases prototype diversity, i.e., the number of distinct top-5 features activated, especially for tail classes. This suggests that the model avoids collapsing onto frequent-class prototypes and learns more diverse, semantically rich representations. These results motivate Dual-centering as an effective strategy for reducing class imbalance effects in representation learning.

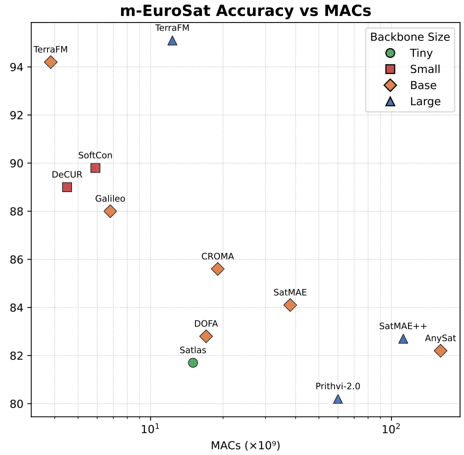

Figure 6: Performance comparison on GEO-Bench using supervised fine-tuning and kNN evaluation. TerraFM consistently outperforms recent EO foundation models, AnySat Astruc et al. (2024), DOFA Xiong et al. (2024), Galileo Tseng et al. (2025), Prithvi-2.0 Szwarcman et al. (2024), and Satlas Bastani et al. (2023), across modalities and evaluation settings.

MACs-Performance Trade-Off: We analyze the compute–accuracy trade-off using Multiply–Accumulate operations (MACs) to measure inference cost. As shown in Fig. 6, TerraFM achieves the highest m-EuroSat accuracy at substantially lower MACs, validating the efficiency of our fusion design and pretraining strategy. Notably, models with higher MACs do not guarantee better performance, underscoring the need for compact yet expressive architectures in scalable EO settings.

For further results and other supporting information, we refer readers to the Appendix.

6 CONCLUSION

In this work, we introduced TerraFM, a unified and scalable foundation model (FM) specifically designed for multisensor EO. Given the unique nature of EO data, our approach pays special treatment to sensor heterogeneity, scale-invariance, and class-frequency imbalance which is critical for building generalizable EO FMs. Our pretraining approach leverages contrastive learning to obtain geographically and spectrally aware representations from large-scale Sentinel-1 and 2 data. Specifically, we integrate modality-specific patch embeddings, adaptive cross-attention fusion, and a dual-centering contrastive learning objective to enrich the representations on heterogeneous RS data. Our extensive evaluations on GEO-Bench and Copernicus-Bench demonstrate that TerraFM consistently outperforms SoTA self-supervised ViT models across both classification and segmentation tasks.

REFERENCES

Guillaume Astruc, Nicolas Gonthier, Clement Mallet, and Loic Landrieu. Anysat: An earth observation model for any resolutions, scales, and modalities. *arXiv preprint arXiv:2412.14123*, 2024.

Cesar Aybar, Lesly Bautista, David Montero, Julio Contreras, Daryl Ayala, Fernando Prudencio, Jhomira Loja, Luis Ysuhuaylas, Fernando Herrera, Karen Gonzales, et al. CloudSEN12+: The largest dataset of expert-labeled pixels for cloud and cloud shadow detection in Sentinel-2. *Data in Brief*, 56:110852, 2024.

Favyen Bastani, Piper Wolters, Ritwik Gupta, Joe Ferdinando, and Aniruddha Kembhavi. Satlaspretrain: A large-scale dataset for remote sensing image understanding, 2023. URL `https://arxiv.org/abs/2211.15660`.

Hylke E Beck, Niklaus E Zimmermann, Tim R McVicar, Noemi Vergopolan, Alexis Berg, and Eric F Wood. Present and future köppen-geiger climate classification maps at 1-km resolution. *Scientific data*, 5(1):1–12, 2018.

Mathilde Caron, Hugo Touvron, Ishan Misra, Hervé Jégou, Julien Mairal, Piotr Bojanowski, and Armand Joulin. Emerging properties in self-supervised vision transformers. In *Proceedings of the IEEE/CVF international conference on computer vision*, pp. 9650–9660, 2021.

Hugo Chan-To-Hing and Bharadwaj Veeravalli. Fus-mae: A cross-attention-based data fusion approach for masked autoencoders in remote sensing. In *IGARSS 2024-2024 IEEE International Geoscience and Remote Sensing Symposium*, pp. 6953–6958. IEEE, 2024.

Kai Norman Clasen, Leonard Hackel, Tom Burgert, Gencer Sumbul, Begüm Demir, and Volker Markl. reBEN: Refined BigEarthNet dataset for remote sensing image analysis. *arXiv preprint arXiv:2407.03653*, 2024.

Yezhen Cong, Samar Khanna, Chenlin Meng, Patrick Liu, Erik Rozi, Yutong He, Marshall Burke, David B. Lobell, and Stefano Ermon. SatMAE: Pre-training transformers for temporal and multi-spectral satellite imagery. In Alice H. Oh, Alekh Agarwal, Danielle Belgrave, and Kyunghyun Cho (eds.), *Advances in Neural Information Processing Systems*, 2022. URL `https://openreview.net/forum?id=WBhqzpF6KYH`.

Rodrigo Caye Daudt, Bertrand Le Saux, Alexandre Boulch, and Yann Gousseau. Urban change detection for multispectral earth observation using convolutional neural networks, 2018. URL `https://arxiv.org/abs/1810.08468`.

Alexey Dosovitskiy, Lucas Beyer, Alexander Kolesnikov, Dirk Weissenborn, Xiaohua Zhai, Thomas Unterthiner, Mostafa Dehghani, Matthias Minderer, Georg Heigold, Sylvain Gelly, Jakob Uszkoreit, and Neil Houlsby. An image is worth 16x16 words: Transformers for image recognition at scale. In *International Conference on Learning Representations*, 2021. URL `https://openreview.net/forum?id=YicbFdNTTy`.

Matthias Drusch, Umberto Del Bello, Sébastien Carlier, Olivier Colin, Veronica Fernandez, Ferran Gascon, Bianca Hoersch, Claudia Isola, Paolo Laberinti, Philippe Martimort, et al. Sentinel-2: Esa's optical high-resolution mission for gmes operational services. *Remote sensing of Environment*, 120:25–36, 2012.

Esri, Global Mapping International, and U.S. Central Intelligence Agency. World Regions. `https://www.arcgis.com/home/item.html?id=84dbc97915244e35808e87a881133d09`, 2025. Layer package representing boundaries for 25 commonly recognized world regions. Updated April 29, 2025. Accessed April 30, 2025.

Radiant Earth Foundation. Crop type classification dataset for western cape, south africa, 2021.

Alistair Francis and Mikolaj Czerkawski. Major tom: Expandable datasets for earth observation. In *IGARSS 2024-2024 IEEE International Geoscience and Remote Sensing Symposium*, pp. 2935–2940. IEEE, 2024.

Anthony Fuller, Koreen Millard, and James Green. Croma: Remote sensing representations with contrastive radar-optical masked autoencoders. *Advances in Neural Information Processing Systems*, 36:5506–5538, 2023.

Peng Gao, Teli Ma, Hongsheng Li, Ziyi Lin, Jifeng Dai, and Yu Qiao. MCMAE: Masked convolution meets masked autoencoders. In Alice H. Oh, Alekh Agarwal, Danielle Belgrave, and Kyunghyun Cho (eds.), *Advances in Neural Information Processing Systems*, 2022. URL `https://openreview.net/forum?id=qm5LpHyyOUO`.

Omid Ghorbanzadeh, Yonghao Xu, Hengwei Zhao, Junjue Wang, Yanfei Zhong, Dong Zhao, Qi Zang, Shuang Wang, Fahong Zhang, Yilei Shi, Xiao Xiang Zhu, Lin Bai, Weile Li, Weihang Peng, and Pedram Ghamisi. The outcome of the 2022 landslide4sense competition: Advanced landslide detection from multisource satellite imagery. *IEEE Journal of Selected Topics in Applied Earth Observations and Remote Sensing*, 15:9927–9942, 2022. doi: 10.1109/JSTARS.2022.3220845.

Xin Guo, Jiangwei Lao, Bo Dang, Yingying Zhang, Lei Yu, Lixiang Ru, Liheng Zhong, Ziyuan Huang, Kang Wu, Dingxiang Hu, et al. Skysense: A multi-modal remote sensing foundation model towards universal interpretation for earth observation imagery. In *Proceedings of the IEEE/CVF Conference on Computer Vision and Pattern Recognition*, pp. 27672–27683, 2024.

Boran Han, Shuai Zhang, Xingjian Shi, and Markus Reichstein. Bridging remote sensors with multisensor geospatial foundation models. In *Proceedings of the IEEE/CVF Conference on Computer Vision and Pattern Recognition*, pp. 27852–27862, 2024.

Michael Schmitt; Lloyd Hughes; Pedram Ghamisi; Naoto Yokoya; Ronny Hänsch. 2020 IEEE GRSS data fusion contest, 2019. URL `https://dx.doi.org/10.21227/rha7-m332`.

Kaiming He, Xinlei Chen, Saining Xie, Yanghao Li, Piotr Dollár, and Ross Girshick. Masked autoencoders are scalable vision learners. In *Proceedings of the IEEE/CVF conference on computer vision and pattern recognition*, pp. 16000–16009, 2022.

Patrick Helber, Benjamin Bischke, Andreas Dengel, and Damian Borth. Eurosat: A novel dataset and deep learning benchmark for land use and land cover classification. *IEEE Journal of Selected Topics in Applied Earth Observations and Remote Sensing*, 2019.

Fantine Huot, R Lily Hu, Nita Goyal, Tharun Sankar, Matthias Ihme, and Yi-Fan Chen. Next day wildfire spread: A machine learning dataset to predict wildfire spreading from remote-sensing data. *IEEE Transactions on Geoscience and Remote Sensing*, 60:1–13, 2022.

Jeremy Irvin, Hao Sheng, Neel Ramachandran, Sonja Johnson-Yu, Sharon Zhou, Kyle Story, Rose Rustowicz, Cooper Elsworth, Kemen Austin, and Andrew Y Ng. Forestnet: Classifying drivers of deforestation in indonesia using deep learning on satellite imagery. *arXiv preprint arXiv:2011.05479*, 2020.

Kartik Kuckreja, Muhammad Sohail Danish, Muzammal Naseer, Abhijit Das, Salman Khan, and Fahad Shahbaz Khan. Geochat: Grounded large vision-language model for remote sensing. In *Proceedings of the IEEE/CVF Conference on Computer Vision and Pattern Recognition*, pp. 27831–27840, 2024.

Nataliia Kussul, Mykola Lavreniuk, Sergii Skakun, and Andrii Shelestov. Deep learning classification of land cover and crop types using remote sensing data. *IEEE Geoscience and Remote Sensing Letters*, 14(5):778–782, 2017.

Alexandre Lacoste, Nils Lehmann, Pau Rodriguez, Evan Sherwin, Hannah Kerner, Björn Lütjens, Jeremy Irvin, David Dao, Hamed Alemohammad, Alexandre Drouin, et al. Geo-bench: Toward foundation models for earth monitoring. *Advances in Neural Information Processing Systems*, 36:51080–51093, 2023.

Issam Laradji, Pau Rodriguez, Freddie Kalaitzis, David Vazquez, Ross Young, Ed Davey, and Alexandre Lacoste. Counting cows: Tracking illegal cattle ranching from high-resolution satellite imagery. *arXiv preprint arXiv:2011.07369*, 2020.

Jihyeon Lee, Nina R. Brooks, Fahim Tajwar, Marshall Burke, Stefano Ermon, David B. Lobell, Debashish Biswas, and Stephen P. Luby. Scalable deep learning to identify brick kilns and aid regulatory capacity. *Proceedings of the National Academy of Sciences*, 118(17), 2021. ISSN 0027-8424. doi: 10.1073/pnas.2018863118. URL `https://www.pnas.org/content/118/17/e2018863118`.

Xuyang Li, Danfeng Hong, and Jocelyn Chanussot. S2mae: A spatial-spectral pretraining foundation model for spectral remote sensing data. In *Proceedings of the IEEE/CVF Conference on Computer Vision and Pattern Recognition*, pp. 24088–24097, 2024.

Oscar Mañas, Alexandre Lacoste, Xavier Giro-i Nieto, David Vazquez, and Pau Rodriguez. Seasonal contrast: Unsupervised pre-training from uncurated remote sensing data. *arXiv preprint arXiv:2103.16607*, 2021.

Kevin Mayer, Benjamin Rausch, Marie-Louise Arlt, Gunther Gust, Zhecheng Wang, Dirk Neumann, and Ram Rajagopal. 3d-pv-locator: Large-scale detection of rooftop-mounted photovoltaic systems in 3d. *Applied Energy*, 310:118469, 2022. ISSN 0306-2619. doi: https://doi.org/10.1016/j.apenergy.2021.118469. URL `https://www.sciencedirect.com/science/article/pii/S0306261921016937`.

Vishal Nedungadi, Ankit Kariryaa, Stefan Oehmcke, Serge Belongie, Christian Igel, and Nico Lang. Mmearth: Exploring multi-modal pretext tasks for geospatial representation learning. In *European Conference on Computer Vision*, pp. 164–182. Springer, 2024.

Mubashir Noman, Muzammal Naseer, Hisham Cholakkal, Rao Muhammad Anwar, Salman Khan, and Fahad Shahbaz Khan. Rethinking transformers pre-training for multi-spectral satellite imagery. In *CVPR*, 2024.

Maxime Oquab, Timothée Darcet, Théo Moutakanni, Huy Vo, Marc Szafraniec, Vasil Khalidov, Pierre Fernandez, Daniel Haziza, Francisco Massa, Alaaeldin El-Nouby, et al. Dinov2: Learning robust visual features without supervision. *arXiv preprint arXiv:2304.07193*, 2023.

Foyez Ahmed Prodhan, Jiahua Zhang, Fengmei Yao, Lamei Shi, Til Prasad Pangali Sharma, Da Zhang, Dan Cao, Minxuan Zheng, Naveed Ahmed, and Hasiba Pervin Mohana. Deep learning for monitoring agricultural drought in south asia using remote sensing data. *Remote sensing*, 13(9):1715, 2021.

Maryam Rahnemoonfar, Tashnim Chowdhury, Argho Sarkar, Debvrat Varshney, Masoud Yari, and Robin Roberson Murphy. Floodnet: A high resolution aerial imagery dataset for post flood scene understanding. *IEEE Access*, 9: 89644–89654, 2021.

Colorado J Reed, Ritwik Gupta, Shufan Li, Sarah Brockman, Christopher Funk, Brian Clipp, Kurt Keutzer, Salvatore Candido, Matt Uyttendaele, and Trevor Darrell. Scale-mae: A scale-aware masked autoencoder for multiscale geospatial representation learning. In *Proceedings of the IEEE/CVF International Conference on Computer Vision*, pp. 4088–4099, 2023.

Ribana Roscher, Marc Russwurm, Caroline Gevaert, Michael Kampffmeyer, Jefersson A Dos Santos, Maria Vakalopoulou, Ronny Hänsch, Stine Hansen, Keiller Nogueira, Jonathan Prexl, et al. Better, not just more: Data-centric machine learning for earth observation. *IEEE Geoscience and Remote Sensing Magazine*, 2024.

Argho Sarkar, Tashnim Chowdhury, Robin Roberson Murphy, Aryya Gangopadhyay, and Maryam Rahnemoonfar. Sam-vqa: Supervised attention-based visual question answering model for post-disaster damage assessment on remote sensing imagery. *IEEE Transactions on Geoscience and Remote Sensing*, 61:1–16, 2023.

Michael Schmitt, Lloyd Haydn Hughes, Chunping Qiu, and Xiao Xiang Zhu. Sen12ms – a curated dataset of georeferenced multi-spectral sentinel-1/2 imagery for deep learning and data fusion, 2019.

Gencer Sumbul, Marcela Charfuelan, Begüm Demir, and Volker Markl. Bigearthnet: A large-scale benchmark archive for remote sensing image understanding. In *IGARSS 2019-2019 IEEE International Geoscience and Remote Sensing Symposium*, pp. 5901–5904. IEEE, 2019.

Daniela Szwarcman, Sujit Roy, Paolo Fraccaro, Þorsteinn Elí Gíslason, Benedikt Blumenstiel, Rinki Ghosal, Pedro Henrique de Oliveira, Joao Lucas de Sousa Almeida, Rocco Sedona, Yanghui Kang, et al. Prithvi-eo-2.0: A versatile multi-temporal foundation model for earth observation applications. *arXiv preprint arXiv:2412.02732*, 2024.

Maofeng Tang, Andrei Cozma, Konstantinos Georgiou, and Hairong Qi. Cross-scale mae: A tale of multiscale exploitation in remote sensing. *Advances in Neural Information Processing Systems*, 36:20054–20066, 2023.

Ramon Torres, Paul Snoeij, Dirk Geudtner, David Bibby, Malcolm Davidson, Evert Attema, Pierre Potin, BjÖrn Rommen, Nicolas Floury, Mike Brown, et al. Gmes sentinel-1 mission. *Remote sensing of environment*, 120:9–24, 2012.

Gabriel Tseng, Anthony Fuller, Marlena Reil, Henry Herzog, Patrick Beukema, Favyen Bastani, James R Green, Evan Shelhamer, Hannah Kerner, and David Rolnick. Galileo: Learning global & local features of many remote sensing modalities. In *Forty-second International Conference on Machine Learning*, 2025.

Leonard Waldmann, Ando Shah, Yi Wang, Nils Lehmann, Adam J Stewart, Zhitong Xiong, Xiao Xiang Zhu, Stefan Bauer, and John Chuang. Panopticon: Advancing any-sensor foundation models for earth observation. *arXiv preprint arXiv:2503.10845*, 2025.

Yanzhao Wang, Yonghua Sun, Xuyue Cao, Yihan Wang, Wangkuan Zhang, and Xinglu Cheng. A review of regional and global scale land use/land cover (lulc) mapping products generated from satellite remote sensing. *ISPRS Journal of Photogrammetry and Remote Sensing*, 206:311–334, 2023.

Yi Wang, Nassim Ait Ali Braham, Zhitong Xiong, Chenying Liu, Conrad M Albrecht, and Xiao Xiang Zhu. Ssl4eo-s12: A large-scale multi-modal, multi-temporal dataset for self-supervised learning in earth observation. *arXiv preprint arXiv:2211.07044*, 2022.

Yi Wang, Conrad M Albrecht, Nassim Ait Ali Braham, Chenying Liu, Zhitong Xiong, and Xiao Xiang Zhu. Decoupling common and unique representations for multimodal self-supervised learning. In *European Conference on Computer Vision*, pp. 286–303. Springer, 2024a.

Yi Wang, Conrad M Albrecht, and Xiao Xiang Zhu. Multi-label guided soft contrastive learning for efficient earth observation pretraining, 2024b.

Yi Wang, Hugo Hernández Hernández, Conrad M Albrecht, and Xiao Xiang Zhu. Feature guided masked autoencoder for self-supervised learning in remote sensing. *IEEE Journal of Selected Topics in Applied Earth Observations and Remote Sensing*, 2024c.

Yi Wang, Zhitong Xiong, Chenying Liu, Adam J Stewart, Thomas Dujardin, Nikolaos Ioannis Bountos, Angelos Zavras, Franziska Gerken, Ioannis Papoutsis, Laura Leal-Taixé, et al. Towards a unified copernicus foundation model for earth vision. *arXiv preprint arXiv:2503.11849*, 2025.

Zhecheng Wang, Rajanie Prabha, Tianyuan Huang, Jiajun Wu, and Ram Rajagopal. Skyscript: A large and semantically diverse vision-language dataset for remote sensing. In *Proceedings of the AAAI Conference on Artificial Intelligence*, volume 38, pp. 5805–5813, 2024d.

Ben G Weinstein, Sergio Marconi, Stephanie Bohlman, Alina Zare, Aditya Singh, Sarah J Graves, and Ethan White. Neon crowns: a remote sensing derived dataset of 100 million individual tree crowns. *BioRxiv*, 2020.

Gui-Song Xia, Jingwen Hu, Fan Hu, Baoguang Shi, Xiang Bai, Yanfei Zhong, Liangpei Zhang, and Xiaoqiang Lu. Aid: A benchmark data set for performance evaluation of aerial scene classification. *IEEE Transactions on Geoscience and Remote Sensing*, 55(7):3965–3981, 2017.

Tete Xiao, Yingcheng Liu, Bolei Zhou, Yuning Jiang, and Jian Sun. Unified perceptual parsing for scene understanding. In *European Conference on Computer Vision*. Springer, 2018.

Zhenda Xie, Zheng Zhang, Yue Cao, Yutong Lin, Yixuan Wei, Qi Dai, and Han Hu. On data scaling in masked image modeling. In *Proceedings of the IEEE/CVF Conference on Computer Vision and Pattern Recognition*, pp. 10365–10374, 2023.

Zhitong Xiong, Yi Wang, Fahong Zhang, Adam J Stewart, Joëlle Hanna, Damian Borth, Ioannis Papoutsis, Bertrand Le Saux, Gustau Camps-Valls, and Xiao Xiang Zhu. Neural plasticity-inspired foundation model for observing the earth crossing modalities. *arXiv e-prints*, pp. arXiv–2403, 2024.

Danlin Yu and Chuanglin Fang. Urban remote sensing with spatial big data: A review and renewed perspective of urban studies in recent decades. *Remote Sensing*, 15(5):1307, 2023.

Jin Z., Lin C., Weigl C., Obarowski J., and Hale D. Smallholder cashew plantations in benin, 2021.

Daniele Zanaga, Ruben Van De Kerchove, Dirk Daems, Wanda De Keersmaecker, Carsten Brockmann, Grit Kirches, Jan Wevers, Oliver Cartus, Maurizio Santoro, Steffen Fritz, et al. Esa worldcover 10 m 2021 v200. 2022.

Xiao Xiang Zhu, Jingliang Hu, Chunping Qiu, Yilei Shi, Jian Kang, Lichao Mou, Hossein Bagheri, Matthias Häberle, Yuansheng Hua, Rong Huang, et al. So2sat lcz42: A benchmark dataset for global local climate zones classification. *arXiv preprint arXiv:1912.12171*, 2019.

APPENDIX

This supplementary material presents additional experiments, analyses, and visualizations that complement the main paper. It includes benchmarks information (A), detailed descriptions & experiments for our multimodal fusion strategies (B), implementation details (C.1) and evaluations on scaling trends with data size (C.2), high resolution benchmarks (C.3), & change detection (C.4), Further more we also provide additional analysis and qualitative figures (D.1). We also report GPU-hour comparisons with comparable methods (D.2), landslide detection (D.3) and visualize the land cover distribution of our dataset using global maps (D.4).

A BENCHMARKS

We evaluate TerraFM on two comprehensive remote sensing benchmarks, **GEO-Bench** and **Copernicus-Bench**, which together cover a wide range of tasks, modalities, and resolutions. **1) GEO-Bench** Lacoste et al. (2023) standardizes evaluation across 12 curated tasks, including 6 classification and 6 segmentation challenges. These datasets are selected for open access and license compliance, and have been harmonized with consistent evaluation settings. While GEO-Bench supports various sensor types (e.g., Landsat-8, Sentinel-2, and hyperspectral sensors), for consistency with our model's pretraining, we restrict the main evaluation to Sentinel-2-based tasks. Specifically, we report results on *m-EuroSAT Helber et al. (2019), m-BigEarthNet Sumbul et al. (2019), m-So2Sat Zhu et al. (2019), m-Brick-Kiln* Lee et al. (2021) (classification) and *m-Cashew-Plantation Z. et al. (2021), m-SA-Crop-Type Foundation (2021)* (segmentation). Additional results on the remaining GEO-Bench datasets, including high-resolution tasks, are provided in Appendix C.3. **2) Copernicus-Bench** Wang et al. (2025) provides 15 downstream tasks aligned with the full Sentinel mission family (Sentinel-1 to Sentinel-5P), and categorizes tasks into three levels: low-level (e.g., cloud detection), mid-level (e.g., land cover segmentation), and high-level (e.g., flood detection or yield prediction). While Copernicus-Bench leverages all Sentinel missions, in this work, we restrict evaluation to tasks using only Sentinel-1 and Sentinel-2 imagery. We evaluate on the following subset: *Cloud-S2 Aybar et al. (2024), EuroSAT-S1 Wang et al. (2024c), EuroSAT-S2 Helber et al. (2019), BigEarthNet-S1 Clasen et al. (2024), BigEarthNet-S2 Clasen et al. (2024), DFC2020-S1 Hänsch (2019), DFC2020-S2 Hänsch (2019), LCZ-S2 Zhu et al. (2019).*

B MULTI-MODAL FUSION STRATEGIES:

We investigate various strategies for multi-modal fusion and report results in Table Ap1 on two benchmark datasets: m-BigEarthNet and m-EuroSat. As a baseline, we evaluate standard DINO training using only Sentinel-2 L2A input (*DINO (S2-L2A)*), which learns unimodal representations. To enable explicit modality-aware learning, we apply a *Multi-Student-Teacher* approach where each modality has its own student and teacher networks, along with an alignment loss between student outputs to enforce cross-modal consistency. This yields consistent gains across both datasets. We also test a more expressive fusion approach, *CrossAttn (Q = 196) Global*, where 196 learned queries (standard for 224×224 image inputs) attend globally to multi-modal tokens immediately after patch embedding. However, this method does not perform well, likely due to excessive parameterization and lack of inductive bias for spatial alignment. Figure Ap1 visually summarizes key fusion strategies evaluated in Table Ap1, including (a) Multi-Student-Teacher, (b) unimodal DINO, and (c) CrossAttn (Q = 196) Global, highlighting their architectural differences and fusion mechanisms. Our proposed approach, *TerraFM-B (Q = 1)*, treats a modality as an augmentation and performs fusion using a single learned spatial query per location. This lightweight attention mechanism yields the best performance among non-ensemble methods. To further analyze architectural choices, we test a variant, *TerraFM-B (ViT PatchEmb)*, where the convolutional patch embedding is replaced by a ViT-S backbone purely for token extraction. While competitive, this setup slightly drops the performance due to increased model complexity and potential overfitting. Finally, our full model, *TerraFM-B (Q = 5)*, employs multiple learned spatial queries to achieve richer fusion between modalities. It achieves the best overall performance, validating the scalability and effectiveness of our fusion design.

	m-BigEarthNet	m-EuroSat
DINO (S2-L2A)	54.6	83.2
Multi-Student-Teacher	55.8	87.8
CrossAttn (Q = 196) Global	52.0	77.1
TerraFM-B (Q = 1)	57.2	89.2
TerraFM-B (ViT PatchEmb)	56.9	87.2
TerraFM-B (Q = 5)	**58.1**	**90.4**

Table Ap1: Ablation study on multi-modal fusion strategies using k-NN evaluation. TerraFM-B with multiple spatial queries (Q = 5) achieves the best performance.

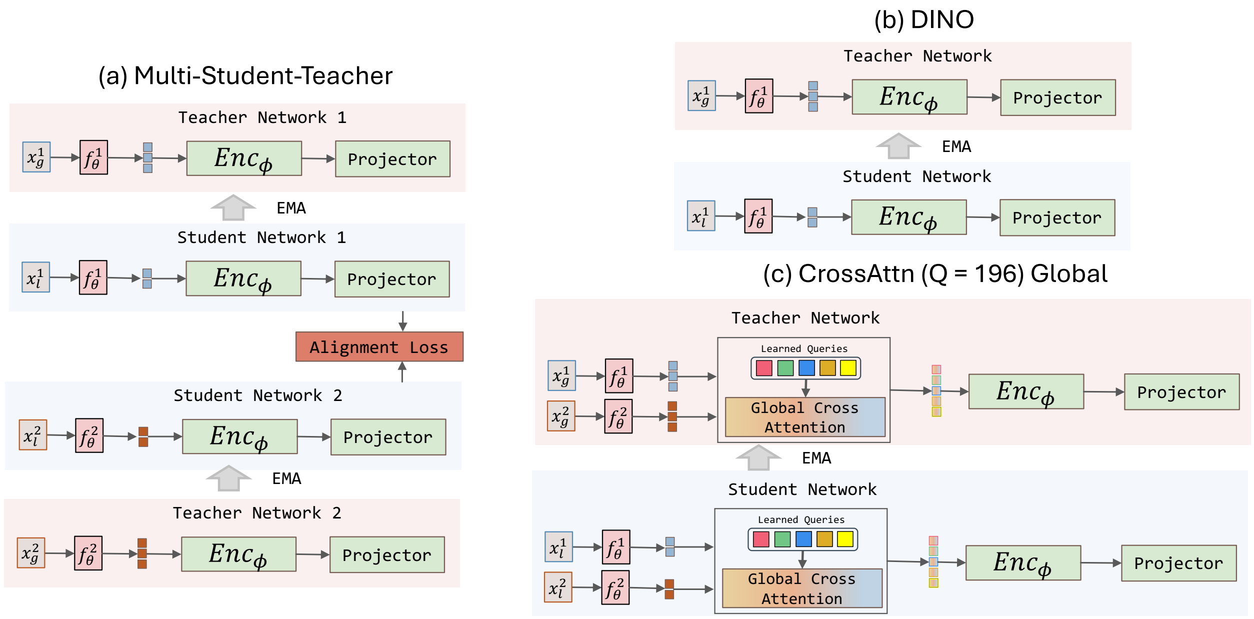
(a) Multi-Student-Teacher

(b) DINO

(c) CrossAttn (Q = 196) Global

Figure Ap1: Architectural overview of different fusion strategies: (a) Multi-Student-Teacher with alignment loss, (b) unimodal DINO baseline, and (c) CrossAttn (Q = 196) with global learned queries.

C EVALUATION

C.1 EVALUATION IMPLEMENTATION DETAILS

Linear Probing Evaluation: To evaluate the quality of learned representations, we follow a linear probing protocol of DINOv2Oquab et al. (2023) that follows with a lightweight grid search over three key hyperparameters: (i) the learning rate, (ii) the number of transformer layers from which features are extracted, and (iii) whether to use only the [CLS] token or to concatenate it with the average-pooled patch tokens. We train the linear classifier using stochastic gradient descent (SGD) for 50 epochs. The training data is augmented using random resized cropping. Specifically, we sweep the learning rate over the set $\{10^{-5},\ 2\times10^{-5},\ 5\times10^{-5},\ 10^{-4},\ 2\times10^{-4},\ 5\times10^{-4},\ 10^{-3},\ 2\times10^{-3},\ 5\times10^{-3},\ 10^{-2},\ 2\times10^{-2},\ 5\times10^{-2},\ 1\}$ Importantly, this search is computationally efficient: features from the frozen backbone are computed once per image using a single forward pass and reused across all configurations, since each linear head only requires a simple forward pass. For each configuration, we evaluate the classifier on the validation set and report the test accuracy achieved by the best validation configuration. **UperNet Probing Evaluation:** For UperNet Xiao et al. (2018) Probing evaluation, we freeze the pretrained backbone and attach `UPerNet` decoder head. Specifically, we use a `Feature2Pyramid` module as the neck, followed by a `UPerNet` decoder and an auxiliary `FCNHead`. We train only the segmentation heads using the AdamW optimizer for 50 epochs without learning rate warm-up. We conduct a grid search over base learning rates $\{10^{-1}, 10^{-2}, 10^{-3}, 10^{-4}, 10^{-5}, 10^{-6}\}$. and batch size set $\{16, 32, 64\}$. **k-NN Evaluation:** To assess the quality of the learned representations without any finetuning, we apply non-parametric classification using a k-nearest neighbors (k-NN) classifier on the frozen features. In addition to sweeping over $k \in 3, 5, 7, 10, 15, 20, 30, 50, 100$ using validation set performance, we follow the same layer selection strategy as linear probing i.e evaluating features from the last 4 transformer layers. This protocol does not require additional training or data augmentation, making it a lightweight and reliable indicator of raw feature quality in pretrained models. **Finetuning Evaluation:** For full-model finetuning, we unfreeze the backbone and jointly optimize it with the task-specific head. We perform a grid search over learning rates in the evaluation set and batch sizes. To stabilize training, we apply a reduced learning rate for the backbone, set to half of the main learning rate used for the head parameters. Once the best configuration is selected based on validation performance, we evaluate the finetuned model on the test set.

C.2 SCALING TRENDS WITH DATASET SIZE:

We report scaling results on four GEO-Bench classification tasks when increasing model size and the pretraining dataset from 20% to 100% (Table Ap2). While all model sizes improve with additional data, the effect is more pronounced

Table Ap2: Scaling behavior of TerraFM models with increasing model size and pretraining data across four GEO-Bench classification tasks.

Dataset	Model	20%	100%	Gain
EuroSat	TerraFM-S	91.7	92.0	0.3
	TerraFM-B	92.0	94.2	2.2
	TerraFM-L	92.1	95.1	3.0
BigEarthNet	TerraFM-S	62.6	65.3	2.7
	TerraFM-B	63.2	68.7	5.5
	TerraFM-L	62.6	69.4	6.8
So2sat	TerraFM-S	50.5	52.3	1.8
	TerraFM-B	49.7	55.1	5.4
	TerraFM-L	49.1	55.9	6.8
Brick-Kiln	TerraFM-S	90.5	91.4	0.9
	TerraFM-B	91.4	94.5	3.1
	TerraFM-L	91.0	93.0	2.0

for the Base and Large variants. For example, TerraFM-L achieves a 6.8 point gain on BigEarthNet and So2Sat, compared to only 2.7 and 1.8 for TerraFM-S. On EuroSat and Brick-Kiln, where performance is already near saturation, the gains are smaller but still positive. These results confirm that larger models are more data-efficient and benefit disproportionately from increased pretraining scale, aligning with scaling laws observed in recent foundation model studies.

C.3 EVALUATION ON HIGH-RESOLUTION BENCHMARKS.

To further assess generalization, we extend TerraFM's evaluation to include low-to-high resolution GEO-Bench tasks as well as the widely used AID Xia et al. (2017) dataset (Table Ap3). Despite being pretrained solely on Sentinel-1 and Sentinel-2, TerraFM achieves consistent improvements over Galileo across diverse sensors and resolutions. Notably, TerraFM transfers effectively to m-forestnet, which uses 15m Landsat-8 inputs compared to TerraFM's 10m Sentinel-2 pretraining resolution, yielding a +7.7 point gain from baseline. On fine-scale RGB datasets such as m-pv4ger (0.1m) and m-chesapeake-landcover (1m), TerraFM also shows strong gains (+1.5 and +36.8 mIoU, respectively). These results highlight TerraFM's robustness across modalities and scales ranging from 0.1–15 m, complementing the evaluations in the main paper.

Table Ap3: Comparison on low-to high resolution benchmarks.

Dataset	Task	Sensor	Resolution	Galileo	TerraFM
m-forestnet (Irvin et al. (2020))	Classification	Landsat 8	15m	49.4	57.1
m-pv4ger (Mayer et al. (2022))	Classification	RGB	0.1m	96.7	98.2
AID (Xia et al. (2017))	Classification	RGB	—	78.2	93.8
m-pv4ger-seg (Mayer et al. (2022))	Segmentation	RGB	0.1m	55.8	85.6
m-chesapeake-landcover (Schmitt et al. (2019))	Segmentation	RGB	1.0m	14.6	51.4
m-nz-cattle (Laradji et al. (2020))	Segmentation	RGB	0.1m	49.7	68.5
m-NeonTree (Weinstein et al. (2020))	Segmentation	RGB	0.1m	51.1	54.0

C.4 EVALUATION ON CHANGE DETECTION.

We evaluate TerraFM on the OSCD Daudt et al. (2018) change detection dataset to assess the effect of sensor-invariance on temporal tasks (Table Ap4). Despite being trained without explicit temporal supervision, TerraFM-B with U-Net probing achieves 52.2 mIoU, substantially outperforming SSL4EO-S12 Wang et al. (2022) (35.1), SEN12MS Schmitt et al. (2019) (30.6), and SeCo Mañas et al. (2021) (28.3). This suggests that TerraFM not only learns robust cross-sensor invariances but also implicitly learns time-invariant representations. However, due to the nature of DINO loss, which aligns global semantics, the model may still preserve object-level distinctions, resulting in improved performance on OSCD.

Table Ap4: Performance comparison on the change detection.

Method	SeCo	SEN12MS	SSL4EO-S12	TerraFM-B
F1 Score (%)	28.33	30.62	35.08	52.20

D ADDITIONAL ANALYSIS

D.1 QUALITATIVE RESULTS:

Fig. Ap2 illustrates qualitative results for the cloud and cloud shadow segmentation task from Copernicus-Bench. TerraFM accurately outlines both cloud and shadow regions, effectively distinguishing visually similar patterns while maintaining spatial coherence across varied scenes.

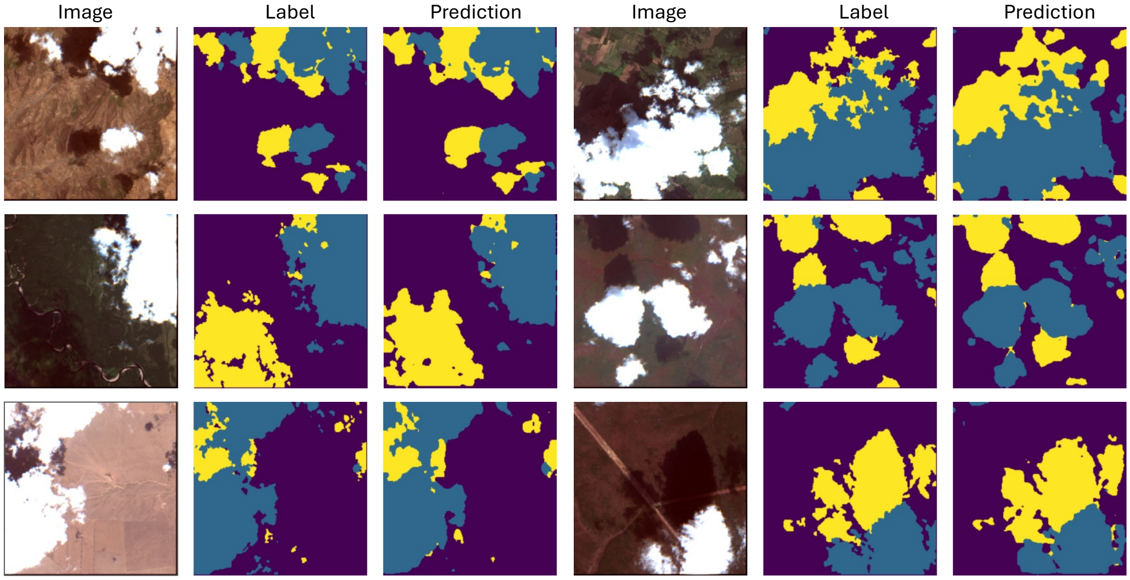

Figure Ap2: Qualitative results for cloud and cloud shadow segmentation. Each triplet shows the input image (left), the ground truth mask (middle), and the TerraFM prediction (right).

D.2 GPU HOUR COMPARISON:

Compared to Prithvi-2.0, which trains ViT-L (300M) model using up to 80 GPUs for 400 epochs, consuming approximately 21,000 GPU-hours Szwarcman et al. (2024), our TerraFM (300M) achieves comparable scale using significantly fewer resources. Specifically, TerraFM is trained for 200 epochs on 64 GPUs, amounting to approximately 12,000 GPU-hours.

D.3 LANDSLIDE DETECTION

We evaluate landslide segmentation on the Landslide4Sense (L4S) Ghorbanzadeh et al. (2022) benchmark, which provides segmentation labels for landslide and non-landslide regions across diverse mountainous areas using multi-source satellite data, including Sentinel-2 bands, DEM, and slope information. Our method, TerraFM, achieves strong performance with a mean IoU of 70.8 and a landslide IoU of 43.1, outperforming the Prithvi-EO-2.0 baseline (Table Ap5). Both TerraFM and Prithvi-EO-2.0 are trained using focal loss with a batch size of 16, Adam optimizer with a learning rate of 1×10^{-4}. Figure Ap3 shows qualitative results from TerraFM, illustrating predicted landslide masks alongside the ground truth.

	mIoU	IoU (Landslide)
Prithvi-EO-2.0 (300M)	65.0	31.5
TerraFM (120M)	**70.8**	**43.1**

Table Ap5: Landslide detection performance on the Landslide4Sense test set. Despite being significantly smaller (120M parameters vs. 300M for Prithvi-EO-2.0), TerraFM achieves higher overall segmentation performance, especially for landslide regions.

D.4 LAND COVER DISTRIBUTION:

Fig. Ap5 illustrates the global spatial coverage of our pretraining data. The selected samples span diverse ecosystems, capturing a balanced mix of urban, vegetation, sea, and arid regions. The insets demonstrate fine-grained land cover variability, ensuring semantic richness across training tiles. This diverse geographic grounding plays a crucial role in enabling the generalization capabilities of TerraFM across regions and tasks.

LLM Usage Statement: We used large language models for polishing and improving the clarity of writing. They were not involved in research ideation, experiment design, analysis, or generation of results.

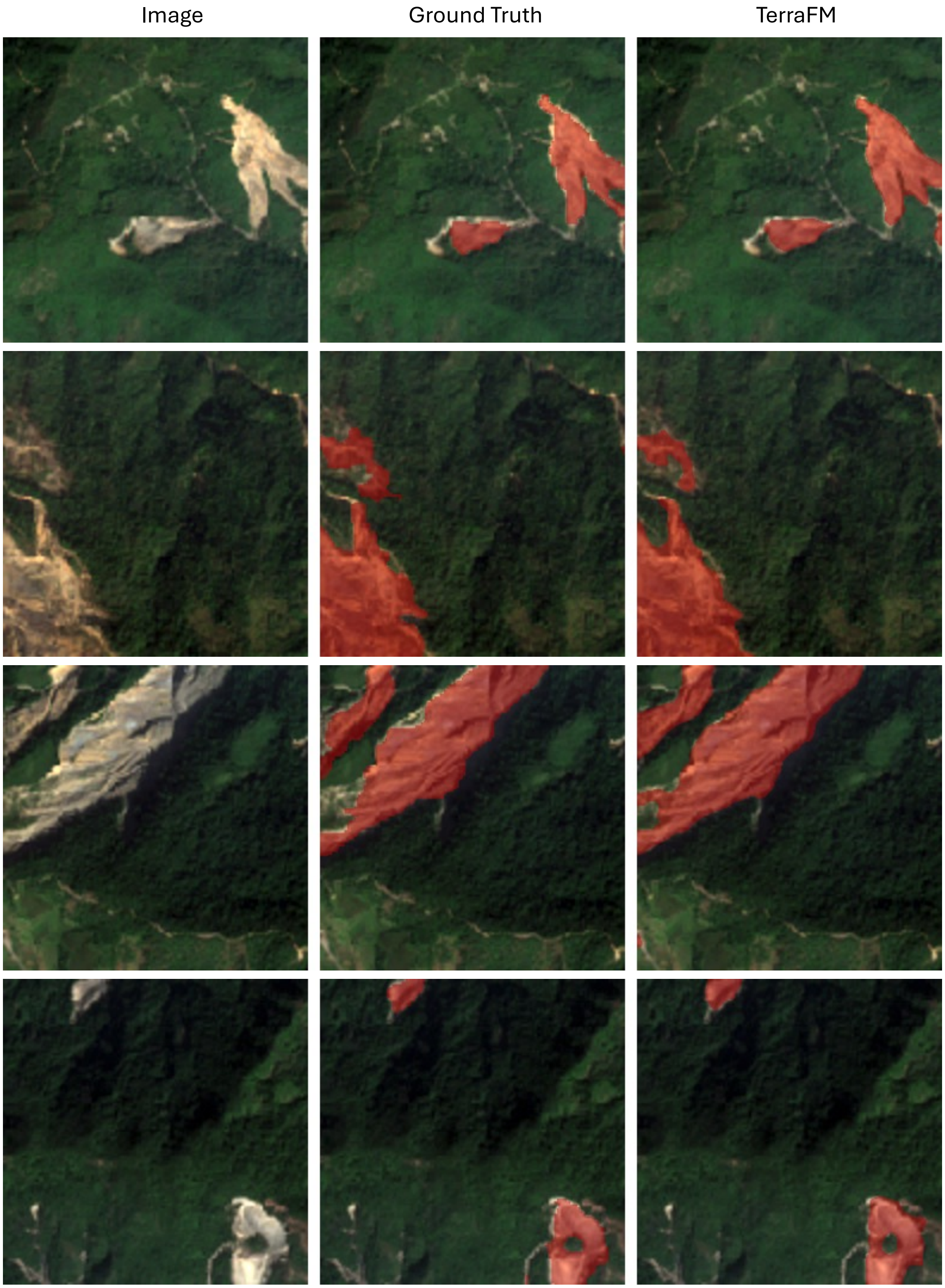

Figure Ap3: Qualitative results for landslide segmentation. Each triplet shows the input image (left), the ground truth mask (middle), and the TerraFM prediction (right).

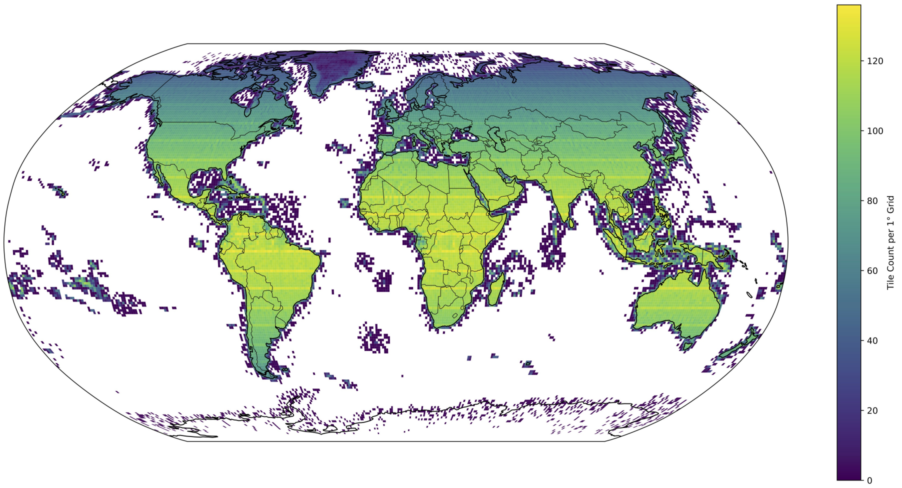

Figure Ap4: Global spatial distribution of the Major-TOM Francis & Czerkawski (2024) training subset. Each square shows a $1^\circ \times 1^\circ$ cell, colored by the number of 10.68 km × 10.68 km tiles it contains.

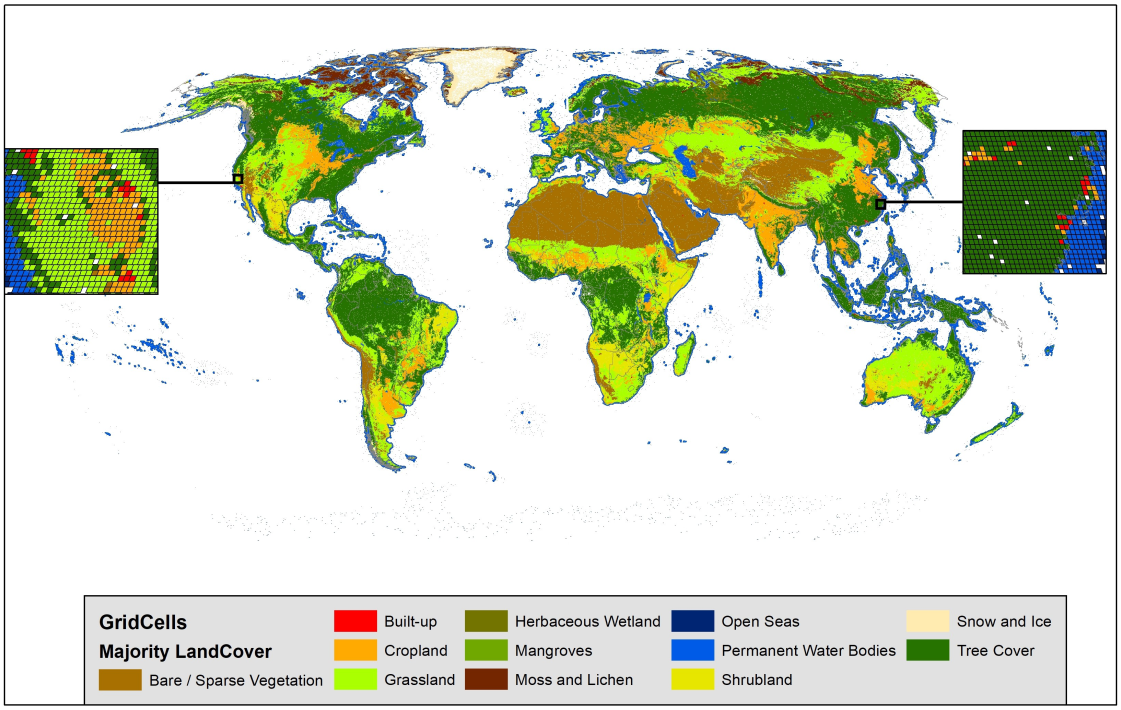

Figure Ap5: Global distribution of sampled training tiles by dominant land cover class, based on ESA WorldCover labels. Insets show detailed tile-level diversity, highlighting coverage across built-up, vegetation, and water classes.